Highly Efficient Analog Maximum Power Point Tracking (AMPPT) in a Photovoltaic System

Chih-Yu Yang, Chun-Yu Hsieh, Fu-Kuei Feng, and Ke-Horng Chen, *Senior Member, IEEE*

***Abstract*—A compact-size analog maximum power point tracking (AMPPT) technique is proposed in this paper for high power efficiency in the photovoltaic (PV) system. Combining existing MPPT approaches, we present a fast and accurate tracking performance. Here, a wide-range current multiplier, which tracks the maximum power point (MPP) in the solar power system, is implemented to detect the power slope condition of the solar panel. Experimental results show that the proposed technique can rapidly track the MPP with a high tracking accuracy of 97.3%. Furthermore, the proposed system can connect to the grid-connected inverter to supply ac power.**

***Index Terms*—Analog Maximum Power Point Tracking (AMPPT), grid-connected inverter, photovoltaic system, tracking efficiency, wide-range current multiplier.**

I. Introduction

THE GLOBAL warming crisis has recently drawn worldwide public attention to issues related to energy conservation and alternative energy. Several energy conservation methods, such as energy recycling [1] and energy harvesting techniques [2], have been proposed to reduce unnecessary energy waste from commercial appliances. In addition, alternative energy, such as thermal [3], wind [4], or solar energy [5], is renewable and addresses pollution problems. Solar energy presents the advantages of low maintenance cost and pollution-free characteristics. These are keys to solving worsening global warming and reducing greenhouse gas emissions. Thus, this alternative energy has been gaining increasing popularity in numerous countries.

Solar energy may not be the most efficient choice with regard to energy production. Nevertheless, it still outweighs other kinds of energy, such as nuclear, coal, and gas energy, because it causes zero pollution, has no moving parts, and allows for easy maintenance. Despite these advantages, the overall energy production cost for solar energy is still too high compared with that incurred from gas or oil production. High costs restrict the wide-ranging global application of solar power systems. Generally, the low power efficiency of a solar power system is attributed to two factors. One is the conversion efficiency of the solar cell. The other is related to the power efficiency of the system, or more specifically, the power efficiency on the power stage. The improvement of solar cell materials and relevant technology has continuously elevated the conversion efficiency of solar cells [6]. Conversion energy is reported to reach around 30% in today's commercial products when a specific material is adopted [7]. Furthermore, enhancing the power efficiency of solar power systems enables the improvement of the efficiency of the power stage and the extraction of substantial energy from solar panels. The nonlinear physical characteristics of solar arrays, however, are inevitable obstacles to the highly efficient energy utilization of solar power systems.

The maximum available power supplied by a solar array depends on solar irradiation level and ambient temperature [8]. In practice, both these factors are difficult to precisely predict and measure. Thus, contemporary photovoltaic (PV) products, such as PV inverters [9] or solar chargers [10], are usually integrated with maximum power point tracking (MPPT) technique to extract the highest energy volume from solar arrays. Several MPPT algorithms exist [11], [12]. Some of them are implemented using a microcontroller [13], field programmable gate array [14], and digital signal processors [15]. Others are implemented using analog or mixed signal methods [16], [17]. For instance, in [18], a small-signal sinusoidal perturbation is injected into the switching frequency to compare the ac component [18]. The average value of the solar array voltage is used to locate the maximum power point (MPP). In [19], the authors track the MPP by introducing a small-signal sinusoidal perturbation into the duty cycle of the switch and comparing the maximum variation in the input voltage and the voltage stress on the switch. Ref. [20] uses the extremum-seeking control method to track the MPP. All of these tracking methods can exhibit high tracking accuracy. Unfortunately, they are implemented by discrete components instead of an integrated circuit (IC). In [21], a dual-module–based tracking technique, which compares the voltage and current difference between two solar arrays to track the MPP, is proposed. This method, however, increases hardware costs because each solar array has to be controlled by an individual tracker.

References [22] and [23] use the pilot cell to assist tracking. Nevertheless, the pilot cell should match the characteristics of the main solar array. In [24], a tracking solution is used to address the problems encountered during rapidly changing weather conditions. The technique incorporates an additional measurement of power in the middle of the MPPT sampling period. Furthermore, one can also use the information of the solar array, such as the diode quality factor and the reverse

Manuscript received May 18, 2011; revised July 27, 2011 and September 14, 2011; accepted October 30, 2011. Date of publication January 17, 2012; date of current version June 22, 2012. This work was supported by the National Science Council, Taiwan, under Grant NSC 100-2220-E-009-050 and NSC 100-2220-E-009-055. This paper was recommended by Associate Editor E. Alarcon.

The authors are with the Institute of Electrical Control Engineering, National Chiao Tung University, Hsinchu 30010, Taiwan (e-mail: khchen@cn.nctu.edu.tw).

Color versions of one or more of the figures in this paper are available online at http://ieeexplore.ieee.org.

Digital Object Identifier 10.1109/TCSI.2011.2177008

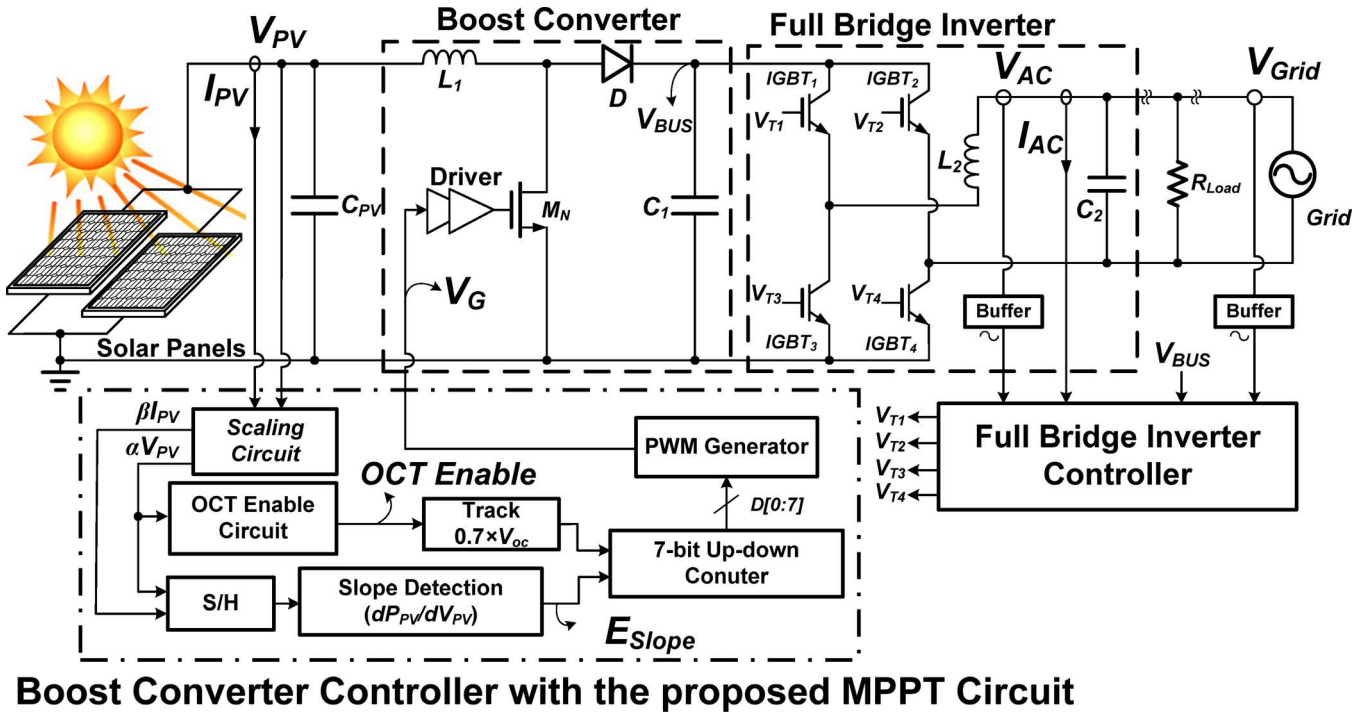

Fig. 1. Proposed grid-connected PV system.

saturation current, to track the MPP [25]. Some methods combine two different tracking techniques to gain advantages. In [26] and [27], two tracking techniques are combined to improve tracking accuracy. The system switches between two tracking methods according to irradiation levels. In the current paper, a MPP tracker using a single-chip controller IC is proposed. The proposed MPP tracker integrates some current-domain arithmetic circuits, sensing circuits, and duty cycle modulation circuits to achieve the MPP calculation. All of the circuits are implemented in a single-chip. The tracker features rapid tracking speed and high tracking accuracy. In addition, the proposed system includes a boost dc-dc converter and a grid-connected PV inverter to enable the transport of solar energy into the power grid for further use [28].

The proposed PV system is illustrated in Fig. 1. The boost converter works in conjunction with the proposed MPPT circuit in consistently tracking the MPP of the solar array. In addition, a full bridge inverter is incorporated to convert dc to ac power.

The rest of the paper is organized as follows. In Section II, the characteristics of the PV module are discussed in detail to show nonlinear behaviors and relevant cause factors. Section III introduces the proposed MPPT algorithm used to extract the highest volume of energy from solar panels. Circuit implementation is presented in Section IV to demonstrate the proposed wide-range current multiplier used in the PV system intended for improving tracking accuracy. The measurement results, shown in Section V, confirm the functionality and efficiency of the proposed MPPT system. Finally, Section VI concludes the paper.

II. Characteristics of the PV Module

As previously mentioned, the characteristics of the PV module vary with different irradiation levels and ambient temperatures. A simplified equivalent circuit [29] in Fig. 2 can facilitate the investigation of the nonlinear behaviors of the PV module. The equivalent circuit consists of a current source I_L, which suggests the light-generated current; a diode D_1, which emulates the PN junction of a real PV cell; a series resistor R_s and a parallel resistor R_p which symbolize the parasitic series resistance and parasitic parallel resistance on the PV module. The voltage generated at terminals $V_{\rm PV}$ is the voltage of the PV module, which can be multiplied through series-connected PV modules. Moreover, the current outflow from terminals $I_{\rm PV}$ is the current of the PV module. The relationship between $V_{\rm PV}$ and $I_{\rm PV}$ can be shown in the following equations [30]:

$$I_{\rm PV} = I_L - I_{os}\left\{\exp\left[\frac{q}{AkT}(V_{\rm PV}+I_{\rm PV}R_s)\right]-1\right\} - \frac{V_{\rm PV}+I_{\rm PV}R_s}{R_P} \quad (1)$$

$$I_{os} = I_{or}\exp\left[\frac{qE_{GO}}{Bk}\left(\frac{1}{T_r}-\frac{1}{T}\right)\right]\left[\frac{T}{T_r}\right]^3 \quad (2)$$

$$I_L = \frac{S\left[I_{SC}+K_I(T-25)\right]}{100} \quad (3)$$

where:

$I_{\rm PV}$	PV module output current;
$V_{\rm PV}$	PV module output voltage;
R_p	parallel resistor;
R_s	series resistor;
I_{os}	PV module reversal saturation current;
A, B	ideality factors;
T	temperature (°C);
k	Boltzmann's constant;

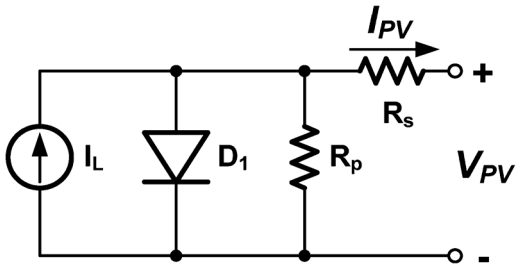

Fig. 2. Equivalent circuit of the PV module.

I_L	light-generated current;
q	electronic charge;
K_I	short-circuit current temperature coefficient at I_{SC};
S	solar irradiation $(\mathrm{W}/\mathrm{m}^2)$;
I_{SC}	short-circuit current at 25°C and 1000 W/m^2;
E_{GO}	bandgap energy for silicon;
T_r	reference temperature;
I_{or}	saturation current at temperature T_r.

The equations verify that the characteristics of the PV module depend on temperature and solar irradiation level. Fig. 3 shows the IV curves plotted under different irradiation levels and ambient temperatures. Under different irradiation levels [Fig. 3(a)], maximum power point P_{MPP} increases nonlinearly as solar irradiation increases. On the other hand, under different ambient temperatures, the characteristics of the IV curves of the solar array behave in the manner depicted in Fig. 3(b). A nonlinear decrease in P_{MPP} is observed when ambient temperature increases. These nonlinear characteristics of the PV module are crucial for analyzing and designing the PV system, especially for the MPP tracker.

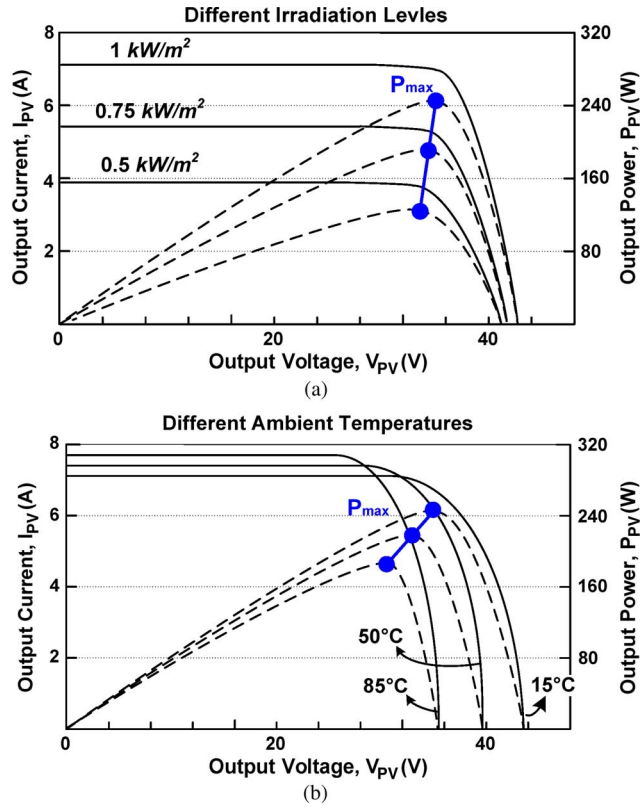

Fig. 3. Characteristic curves under (a) different irradiation levels and (b) ambient temperatures.

III. Proposed MPPT Algorithm

Fig. 4 demonstrates the concept of the proposed MPPT algorithm. Before the solar power system is activated, the operating point of the system is located on open-circuit voltage point V_{OC}. Conventional MPPT algorithms, such as slope detection algorithm [31] [e.g., perturbation and observation (P&O) algorithm or hill-climbing (HC) algorithm], calculate the slope of the characteristic curves to determine slope conditions and track the MPP. Nevertheless, a PV system adopting this algorithm requires a lengthy amount of time to track the operating point from V_{OC} to MPP during the system power-on period, as depicted in Fig. 4.

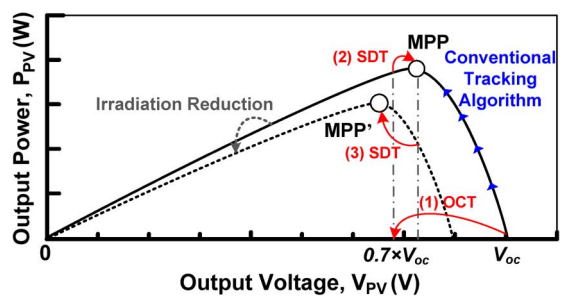

Fig. 4. Illustration of the proposed MPP tracking algorithm.

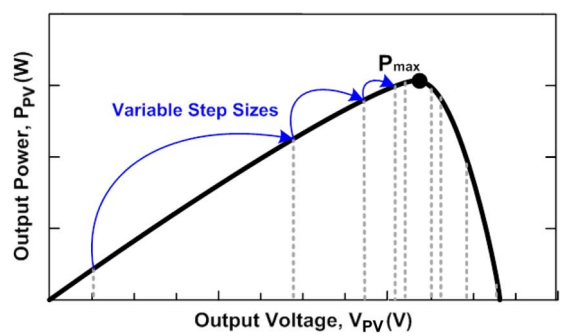

Fig. 5. Illustration of the variable step perturbation (VSP) technique.

Other tracking algorithms such as the constant voltage algorithm use a fixed ratio of maximum power voltage to open-circuit voltage V_{OC} to approximate the MPP. Theoretically, 0.7 fractions of open-circuit voltage V_{OC} is close to the MPP [32]. Therefore, periodically disconnecting the solar array and power stage to measure V_{OC} and multiplying it to 0.7 can rapidly detect the current MPP. The fraction factor (0.7) varies when different solar cell materials are used. Moreover, it is considerably susceptible to environmental conditions such as ambient temperature and solar irradiation level. In this sense, the MPP cannot be guaranteed when varying environmental conditions are taken into consideration. Moreover, consistent disconnection between

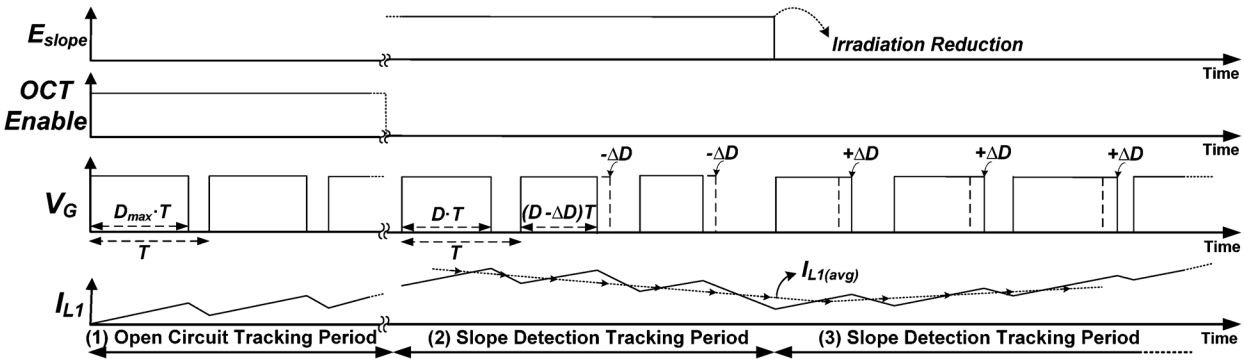

Fig. 6. Timing diagram of the proposed MPP tracking algorithm.

the solar array and power stage causes power delivery interruption during the sampling period, thereby resulting in the low power efficiency of the PV system.

To increase tracking speed and accuracy while maintaining high power efficiency, the open-circuit tracking (OCT) and slope detection tracking (SDT) algorithms are adopted to track the MPP in this study. Disconnection between the solar array and power stage occurs only once; that is, at the beginning of the system power-on period. This way, unnecessary power loss is avoided and the power efficiency is maintained. Fig. 6 illustrates the timing diagram of the proposed tracking algorithm. E_{slope} is a digital signal meant to indicate the slope condition. Logic-high E_{slope} means that the slope condition $dP_{\rm PV}/dV_{\rm PV}$ of the solar array is positive. By contrast, logic-low E_{slope} means $dP_{\rm PV}/dV_{\rm PV}$ is negative. *OCT Enable* indicates whether the OCT algorithm is enabled. V_G is the gate signal of the power NMOS in the boost converter. Signal I_{L1} shows the inductor current of the boost converter, which can also indicate the current of the solar array.

The tracking procedure can be divided into the following sequences. First, before the solar power system is activated, V_{OC} is detected by the controller to set the solar array voltage $V_{\rm PV}$ close to $0.7 \times V_{OC}$. This approach improves tracking speed unlike the slow tracking speeds in conventional P&O and HC algorithms. The switching duty cycle of the boost converter is set to its maximum value to accelerate the tracking speed during the open-circuit voltage detection period. Second, after the OCT period, the SDT technique takes over the tracking procedure to continually and accurately track the MPP, ensuring that the power stage receives the most energy from the solar array. Third, when environmental conditions change (e.g., reduction in irradiation level), the slope condition changes from positive to negative, as indicated by the solar cell characteristics shown in Fig. 3. Then, E_{slope} transits from high to low. As mentioned in Section II, PV voltage tends to decrease as PV current increases, and vice versa. Thus, the SDT technique increases the switching duty cycle. The current of the solar array increases to reduce the operating voltage and ensure the movement of the system operating point to a new maximum power point MPP', as illustrated in Fig. 4. The flowchart in Fig. 6 summarizes the overall tracking topology of the proposed MPP tracking algorithm. After the solar power system is switched on, the OCT technique is enabled until the operating voltage is set to

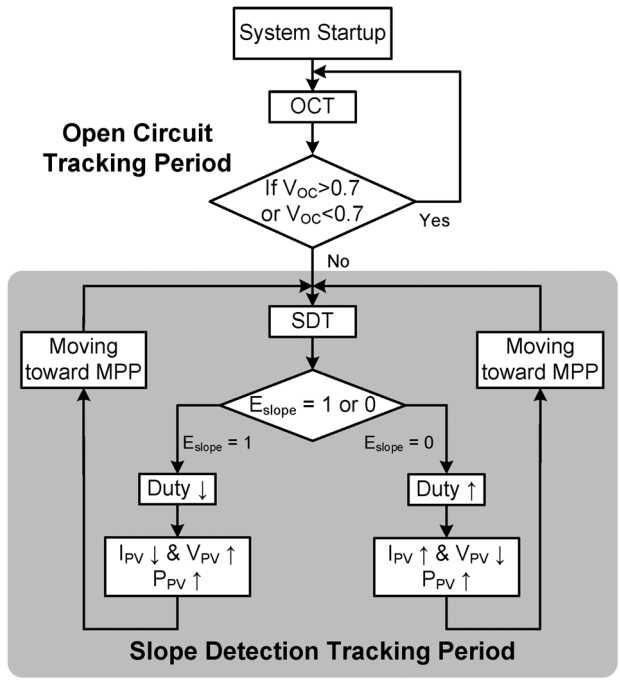

Fig. 7. Flowchart of the proposed MPPT algorithm.

$0.7 \times V_{OC}$. Subsequently, the SDT technique consistently monitors the slope condition and guarantees that the system operates at the MPP regardless of any environmental change.

Besides, the SDT algorithm includes the variable step perturbation (VSP) technique [Fig. 5] to accelerate the tracking speed and to minimize the oscillation problem around the MPP. The system chooses larger perturbation step sizes when the operating point is far away from the MPP, which can increase the tracking speed. In contrast, when the operating point is working around the MPP, the step sizes are set to be smaller in order to minimize the oscillation problem around the MPP.

The proposed AMPPT technique includes the advantages of both the OCT and SDT techniques. The OCT technique can roughly locate the MPP at rapid tracking speeds, while the SDT technique can improve tracking accuracy, which cannot be guaranteed solely by the OCT technique.

For a large-scale PV system, unavoidable shadows caused by nearby trees, clouds, and buildings frequently degrade the energy of the solar array. The so-called “partial shading effect”

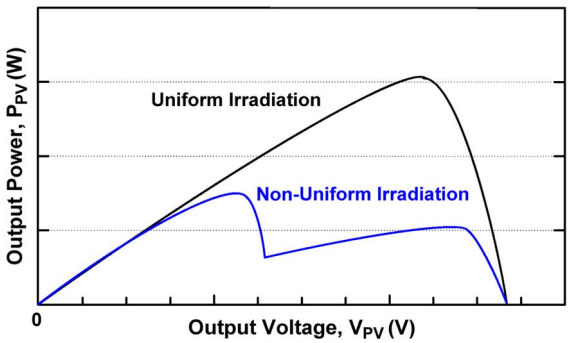

Fig. 8. Power-voltage characteristic curve due to non-uniform irradiation.

[33] poses a considerable threat to highly efficient energy utilization. Fig. 8 shows that when the solar arrays are shaded, there might be local maxima in the IV curves of the solar arrays when the bypass diodes are used. As a result, the designed MPP tracker may easily misjudge the optimal operating point; therefore, the system cannot provide its maximal energy. The proposed MPP tracking algorithm can further be improved by the algorithm described in Fig. 9 to guarantee the robustness of the PV system. The system primarily determines whether it has reached its local maximum power point $(LMPP)$. The measured power (P_{mpp_last}) and voltage (V_{mpp_last}) are then stored for later comparison. The control loop enters the global maximum power point tracking (GMPPT) stage when triggered by the timer. The default timer is set to 1 s. That is, the global maximum power point (GMPP) tracker is enabled every second to check whether the current operating point belongs to the GMPP. If the current operating point is already the maximum point on the power-voltage plane, the system will continuously operate at this point. Otherwise, the GMPP tracker locates the GMPP and forces the system to operate on the located point. During the GMPPT stage, the system is perturbed by a voltage difference $\Delta V_{\text{perturb}}$, which is approximated to 60%–70% of V_{oc} [34]. Thus, an GMPPT technique guarantees full robustness of the connected PV system. Nevertheless, because tracking takes more time to locate the GMPP, the overall tracking speed is downgraded at the circumstance of partial shading. However, high tracking accuracy can be retained because the same SDT technique is used to track the MPP.

$$\eta = \frac{P_{\text{solar}} - P_{\text{loss}} - P_{\text{LMPP}} - f_{\text{GMPPT}} \times (P_{cal} + P_{\text{perturb}})}{P_{\text{solar}}}. \tag{4}$$

The overall power efficiency is undermined when the GMPPT is activated, as shown in (4). P_{solar} denotes all the energy generated from the solar arrays. P_{loss} is the power loss on the power stage. P_{LMPP} denotes the power loss due to the local MPP tracking, which is inversely proportional to the tracking accuracy. f_{GMPPT} is the frequency of the GMPPT procedure. P_{cal} and P_{perturb} are the power consumed by the calculation and perturbation circuits in the GMPPT controller, respectively. As a result, more often the GMPPT is triggered, more energy is wasted and the lower overall power efficiency is presented.

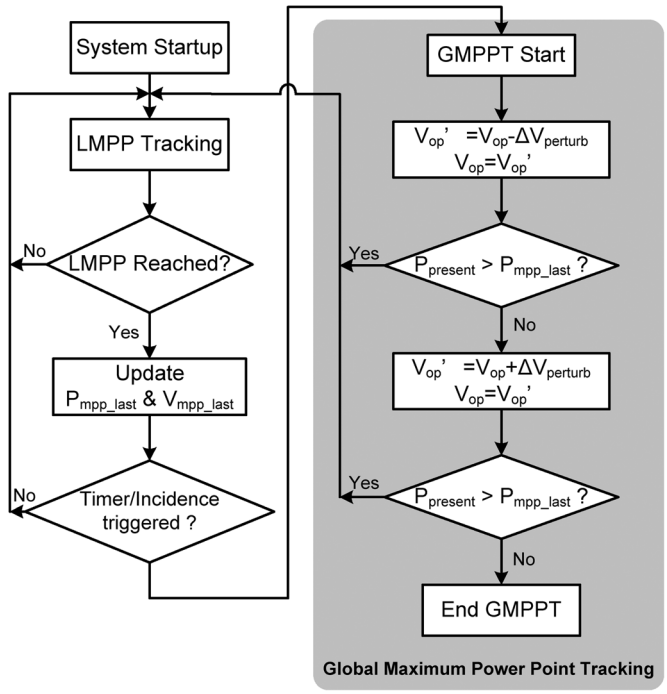

Fig. 9. Flowchart of GMPPT.

IV. Proposed Circuit of the MPPT Controller

The proposed slope detection circuit shown in Fig. 10 detects the slope of the characteristic IV curve, that is, $dP_{\text{PV}}/dV_{\text{PV}}$, at the operating point. The slope equation, according to the transfer curve of power-voltage, can be written as (5).

$$\begin{aligned}\frac{\partial P_{\text{PV}}}{\partial V_{\text{PV}}} &= \frac{\partial (V_{\text{PV}} \cdot I_{\text{PV}})}{\partial V_{\text{PV}}} \\ &= \frac{\partial V_{\text{PV}}}{\partial V_{\text{PV}}} \cdot I_{\text{PV}} + V_{\text{PV}} \cdot \frac{\partial I_{\text{PV}}}{\partial V_{\text{PV}}} \\ &= I_{\text{PV1}} + V_{\text{PV1}} \cdot \frac{I_{\text{PV2}} - I_{\text{PV1}}}{V_{\text{PV2}} - V_{\text{PV1}}} \\ &= I_{\text{PV1}} - V_{\text{PV1}} \cdot \frac{I_{\text{PV1}} - I_{\text{PV2}}}{V_{\text{PV2}} - V_{\text{PV1}}} \\ &= I_{\text{PV1}} - V_{\text{PV1}} \cdot \frac{\Delta I_{\text{PV}}}{\Delta V_{\text{PV}}}. \end{aligned} \tag{5}$$

The denominator in (5) is eliminated deliberately by the conversion ratio of voltage-to-current (V-to-I) converter to improve the calculation accuracy of the slope detection circuit. The slope detector detects the voltage and current information at two different time intervals. They are $(I_{\text{PV1}}, V_{\text{PV1}})$ at $\text{time} = t_1$ and $(I_{\text{PV2}}, V_{\text{PV2}})$ at $\text{time} = t_2$. Utilizing the sample/hold (SH) circuit to sense the photovoltaic voltage and current of solar array, V_{PV1} and I_{PV1} represent the instant photovoltaic voltage and current of solar array, respectively. Similarly, V_{PV2} and I_{PV2} record the previous photovoltaic voltage and current, respectively. For easy and fast operation in analog circuits, the value of $(V_{\text{PV1}}/\Delta V_{\text{PV}})$ is converted to a current signal, I_{VPV1}, by the voltage-to-current (V-to-I) converter, as shown in (6). The coefficient k denotes the conversion gain of the V-to-I converter.

$$\frac{\partial P_{\text{PV}}}{\partial V_{\text{PV}}} = I_{\text{PV1}} - k \cdot I_{\text{VPV1}} \cdot \Delta I_{\text{PV}}. \tag{6}$$

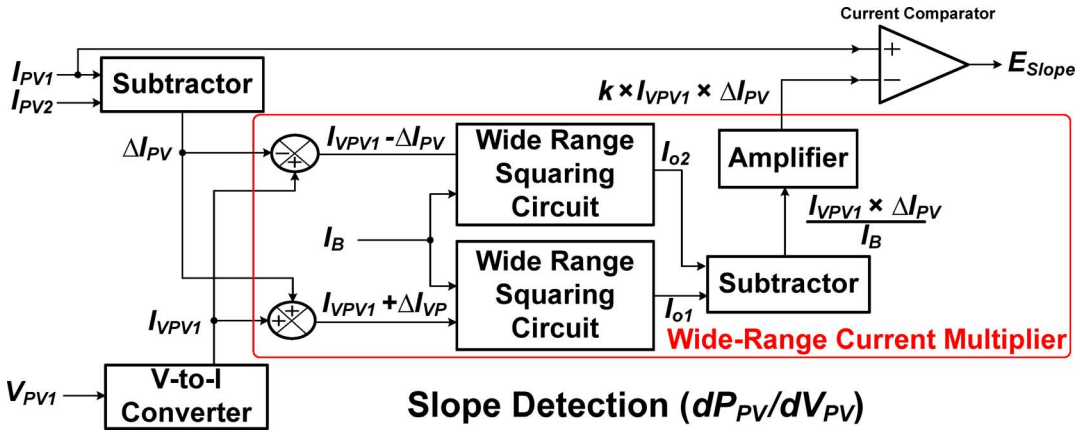

Fig. 10. Proposed slope detection circuit.

The current difference, $\Delta I_{\rm PV}$, between $I_{\rm PV1}$ and $I_{\rm PV2}$, can be derived by the current subtractor. Moreover, the multiplication of $I_{\rm VPV1}$ and $\Delta I_{\rm PV}$, can be achieved by the proposed wide-range current multiplier.

It's obvious from Fig. 4 that the maximum power point occurs at the point where the slope is zero or near to zero. Therefore, one can try to find an operating point whose slope is as low as possible, no matter it is negative or positive. Once this point is found, the maximum power point can then be decided. Nevertheless, there is a simpler way to do the tracking. Observing the characteristic curve of solar array in Fig. 4, the maximum power point falls right between the right-hand side plane and the left-hand side plane of the curve. Namely, the maximum power point occurs on the slope transition point, where slope changes from either positive to negative or from negative to positive. Comparing the current $I_{\rm PV1}$ and $k \times (I_{\rm VPV1} \times \Delta I_{\rm PV})$ in (6), therefore, one can determine the slope condition of solar array, which can be easily carried out by a current comparator.

Fig. 10 shows the block diagram of the proposed slope detection circuit following (6). The slope detection circuit includes a current subtractor, a voltage-to-current converter, a current comparator, and a wide-range current multiplier. The current subtractor serves the purpose of computing the current difference between $I_{\rm PV1}$ and $I_{\rm PV2}$. The output current of the current subtractor is $\Delta I_{\rm PV}$. The voltage-to-current converter is used to convert the voltage data $V_{\rm PV1}$ into the current data $I_{\rm VPV1}$ for further calculation need. The wide-range current multiplier multiplies $\Delta I_{\rm PV}$ and $I_{\rm VPV1}$. In the end, the current comparator compares $I_{\rm PV1}$ and $k \times (I_{\rm VPV1} \times \Delta I_{\rm PV})$ to determine the slope condition and sends out a digital signal, either high or low, to indicate the slope condition at that time instance.

The digital signal E_{slope} indicates the slope condition for the duty cycle modulation circuit, which is made up by a 7-bit up-down counter. The duty cycle modulation circuit increases or decreases the duty cycle of the boost converter. As mentioned before, the voltage of solar array increases nonlinearly as the current decreases, and vice versa. When the slope is positive, the value of E_{slope} is high to decrease the duty cycle of the converter and thus increase the operating voltage. On the other hand, a low value of the E_{slope} indicates the slope is negative. Then the duty cycle increases to decrease the operating voltage.

Since the characteristic of solar array follows majorly by the environmental factors, such as the temperature and the irradiation, the voltage and current range of solar array are very wide. As a result, typical current multipliers cannot meet the need in the PV application. As can be seen in Fig. 10, the proposed wide-range current multiplier is composed of the wide-range squaring circuit, current subtractor and amplifier. The proposed wide-range squaring circuit in the wide-range current multiplier consists of a high current (HI) processor and a low current (LI) processor. This wide-range squaring circuit serves the purpose of extending the allowable current range of the current multiplier. Fig. 11 shows the transistor level of the wide-range current squaring circuit. All the current mirrors are implemented in the cascade way to improve the calculation accuracy. The current comparator in the figure decides whether the input current, $I_{\rm VPV1} + \Delta I_{\rm PV}$, is larger or smaller than the reference current, I_{ref}. If $(I_{\rm VPV1} + \Delta I_{\rm PV})$ is larger than I_{ref}, the HI processor is activated and the current, $(I_{\rm VPV1} + \Delta I_{\rm PV})$ flows into the drain terminal of MOSFET M_{HI3}. After that, the current mirror produces current equal to $2 \times (I_{\rm VPV1} + \Delta I_{\rm PV})$ flowing out from the source terminal of M_{HI3}. By Kirchhoff's Voltage Law (KVL), the summation of $V_{\rm GS,MHI1}$ and $V_{\rm GS,MHI3}$ is equal to that of $V_{\rm GS,MHI2}$ and $V_{\rm GS,MHI4}$ as expressed in (7).

$$V_{\rm GS,MHI1} + V_{\rm GS,MHI3} = V_{\rm GS,MHI2} + V_{\rm GS,MHI4}. \quad (7)$$

The squaring principle of MOSFET gives

$$I_{\rm DS} = K(V_{\rm GS} - V_t)^2 \quad (8)$$

$$V_{\rm GS} = V_t + \sqrt{\frac{I_{\rm DS}}{K}}. \quad (9)$$

where $K = (1/2)\mu_0 C_{ox}(W/L)$ is the transconductance parameter of transistor, $I_{\rm DS}$ is the current flowing through the transistor, $V_{\rm GS}$ is the voltage between gate and source, and V_t is the threshold voltage of the transistor.

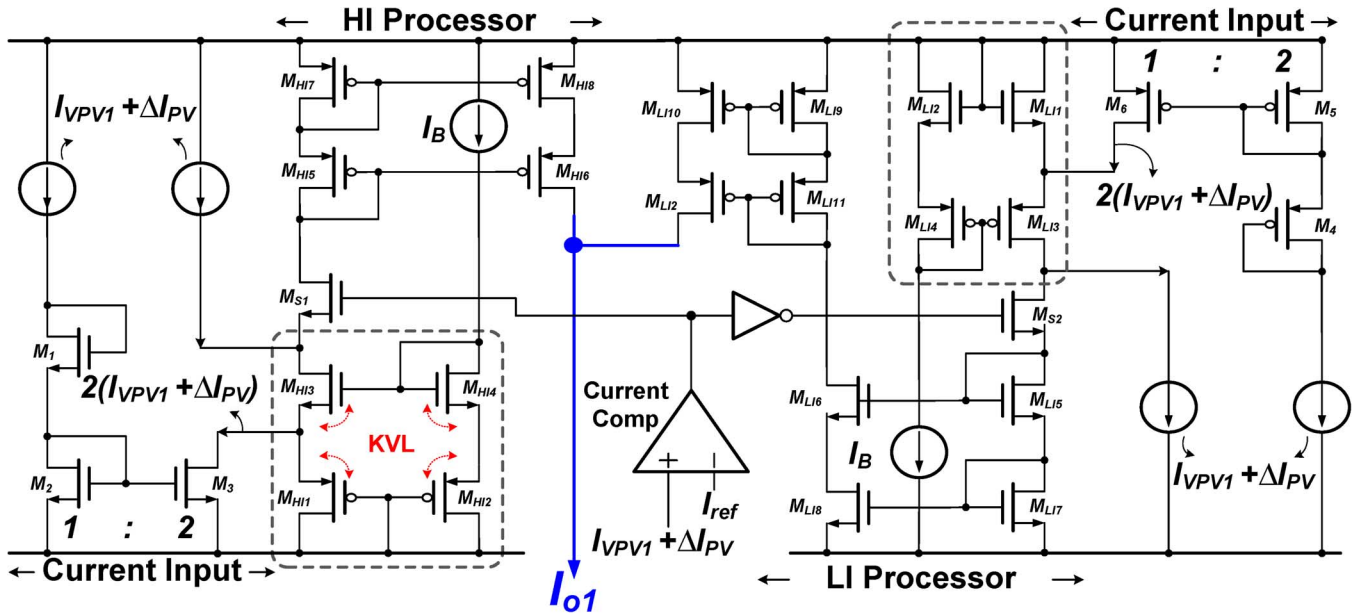

Fig. 11. Proposed wide-range squaring circuit.

Based on squaring principle of transistor in (9), the following equations can be derived from (7).

$$\left(V_t+\sqrt{\frac{I_{\mathrm{MHI1}}}{K}}\right)+\left(V_t+\sqrt{\frac{I_{\mathrm{MHI3}}}{K}}\right) = \left(V_t+\sqrt{\frac{I_{\mathrm{MHI2}}}{K}}\right)+\left(V_t+\sqrt{\frac{I_{\mathrm{MHI4}}}{K}}\right) \tag{10}$$

$$\sqrt{I_{\mathrm{MHI1}}}+\sqrt{I_{\mathrm{MHI3}}} = \sqrt{I_{\mathrm{MHI2}}}+\sqrt{I_{\mathrm{MHI4}}}. \tag{11}$$

Furthermore, according to Kirchhoff's Current Law (KCL), the following equations can therefore be derived.

$$I_{\mathrm{MHI3}} = I_{o1}+(I_{\mathrm{VPV1}}+\Delta I_{\mathrm{PV}}) \tag{12}$$

$$I_{\mathrm{MHI1}} = I_{o1}-(I_{\mathrm{VPV1}}+\Delta I_{\mathrm{PV}}) \tag{13}$$

$$I_{\mathrm{MHI2}} = I_{\mathrm{MHI4}} = I_B. \tag{14}$$

I_B stands for the bias current in the squaring circuit. Substituting (12), (13), and (14) into (11),

$$\sqrt{I_{o1}-(I_{\mathrm{VPV1}}+\Delta I_{\mathrm{PV}})}+\sqrt{I_{o1}+(I_{\mathrm{VPV1}}+\Delta I_{\mathrm{PV}})} = 2\sqrt{I_B}. \tag{15}$$

Squaring both sides, one can derive

$$4I_B = (I_{\mathrm{VPV1}}+\Delta I_{\mathrm{PV}})+I_{o1}+I_{o1}-(I_{\mathrm{VPV1}}+\Delta I_{\mathrm{PV}}) +2\sqrt{I_{o1}^2-(I_{\mathrm{VPV1}}+\Delta I_{\mathrm{PV}})^2}. \tag{16}$$

Eliminating $(I_{\mathrm{VPV1}}+\Delta I_{\mathrm{PV}})$ and squaring both sides again,

$$16I_B^2-16I_BI_{01}+4I_{o1}^2 = 4(I_{\mathrm{VPV1}}+\Delta I_{\mathrm{PV}})^2. \tag{17}$$

Then, the following equation can be derived.

$$I_{01} = \frac{(I_{\mathrm{VPV1}}-\Delta I_{\mathrm{PV}})^2}{4I_B}+I_B. \tag{18}$$

Likewise, another identical wide-range squaring circuit can derive I_{o2} in Fig. 10, where the input current is $(I_{\mathrm{VPV1}}-\Delta I_{\mathrm{PV}})$, as shown in (19).

$$I_{o2} = \frac{(I_{\mathrm{VPV1}}-\Delta I_{\mathrm{PV}})^2}{4I_B}+I_B. \tag{19}$$

Subtracting I_{o2} from I_{o1}, $k\times(I_{\mathrm{VPV1}}\times\Delta I_{\mathrm{PV}})$ can be obtained by amplifying the current $(I_{\mathrm{VPV1}}\times\Delta I_{\mathrm{PV}})/I_B$. E_{slope} is generated in the end to adjust the duty cycle of the boost converter. Accordingly, the operating voltage of solar array is ensured to locate at the maximum power point.

The proposed wide range squaring circuit and the slope detection circuit can precisely determine the slope condition at any time instant and under any circumstance. The boost converter and other controlling circuits in the controller, then, use the detected slope information to manipulate the operating point of the PV system. For that, the PV system can continuously operate under maximum power condition and with high power conversion ratio.

V. Experimental Results

The test chip, which contains both the proposed MPPT circuit and the controller for the boost controller, was fabricated by a 0.25 μm BiCMOS-DMOS (BCD) 40 V 1P4M process. Fig. 12 shows the experimental setup, prototype, and chip micrograph of the controller for the boost converter. The solar array used in the measurement is Tynsolar TYN-285P6 [35]. Table I provides the technical specifications of the solar array.

The tracking accuracy of the MPPT circuit can be estimated using the following equation [36]:

$$\eta_{\mathrm{MPP}} = \frac{P_{\mathrm{PV,tracked}}}{P_{\mathrm{PV,max}}}\times 100\%. \tag{20}$$

$P_{\mathrm{PV,tracked}}$ is the actual energy captured and delivered by the system from the solar array. $P_{\mathrm{PV,max}}$ denotes the maximum energy from the sun at a specific time instance, temperature,

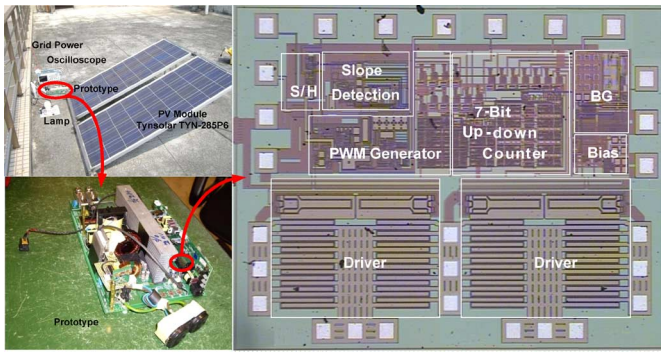

Fig. 12. Experimental prototype and chip micrograph.

TABLE I
TECHNICAL SPECIFICATIONS OF TYN-285P6

Maximum power	285 W
Tolerance	±5%
Open-circuit voltage	44.21 V
Short-circuit current	8.32 A
Maximum power voltage	36.79 V
Maximum power current	7.75 A
Module efficiency	14.61%
Solar cell efficiency	16.37%
Operating temperature	–40 to 85 °C
Short-circuit current temperature coefficient	+4.500 mA/°C
Open-circuit Voltage temperature coefficient	–0.1500 V/°C
Maximum power temperature coefficient	–0.4982 %/°C

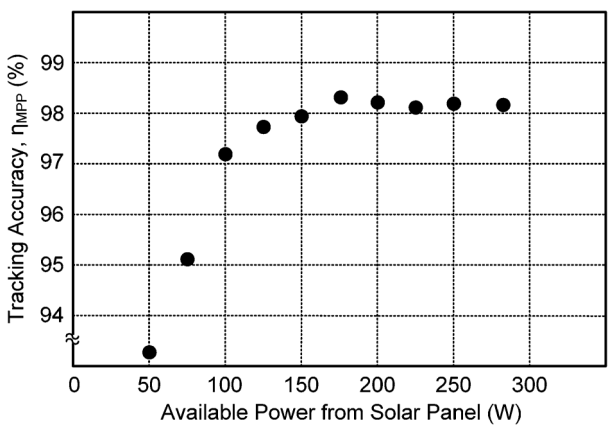

Fig. 13. Tracking accuracy of the proposed MPPT algorithm and circuit.

and solar irradiation. Fig. 13 shows the MPPT accuracy performance measured using the proposed tracking algorithm and circuit. The tracking accuracy is higher than 97.3% in the available power range of 100 to 300 W at ambient temperature of 28°C. The tracking accuracy is limited below 98% compared with that observed in contemporary products [37] because of the following factors: the process variation during the silicon fabrication, temperature variation, IC layout optimization, and limited operation range of the calculation circuit components such as the multiplier, adder, and subtractor. An overflow or underflow current may cause the circuit to misinterpret the slope condition. As a result, tracking accuracy is undermined.

Fig. 14 shows the waveforms of the PV system during the power-on period. At the time that the PV system is switched on, the OCT technique is enabled to adjust the operating voltage close to the value of $0.7 \times V_{OC}$. During this open-circuit voltage

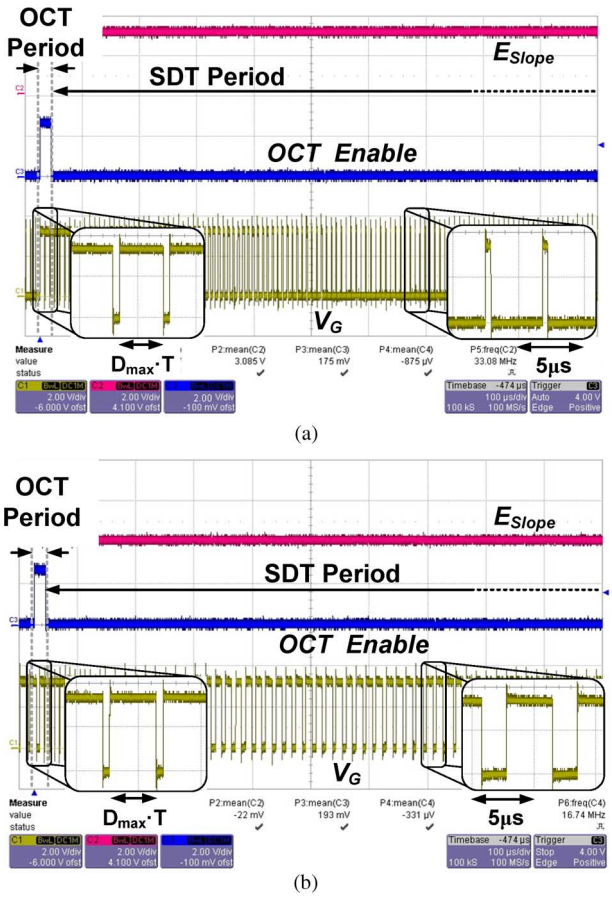

Fig. 14. Waveforms of PV system during the system power-on perio d: (a) when the detected slope condition is positive and (b) when the detected slope condition is negative.

detection period, the duty cycle is set to its maximum value to enhance the tracking speed. After this, the SDT technique takes over the tracking procedure to improve the tracking accuracy. When the slope detection circuit detects that the slope condition is positive (i.e., E_{slope} is high), the duty cycle decreases [Fig. 14(a)]. Consequently, the inductor current is reduced and the operating voltage toward the MPP is increased. Conversely, when the slope condition is detected as negative, E_{slope} is set low and the controller increases the duty cycle to the boost converter [Fig. 14(b)]. As a result, the inductor current increases to lower the operating voltage of the system.

Fig. 15 shows the duty cycle transitions when solar irradiation changes. The detected slope condition changes either from negative to positive or from positive to negative depending on the solar irradiation level. Fig. 15(a) illustrates that when the solar irradiation level increases, the duty cycle of the control signal, V_G, which controls the gate of the power NMOS (M_N), gradually decreases to a smaller value. By contrast, V_G changes from a small to a large duty cycle when the detected slope condition transits from positive to negative, which is caused by the degradation of the solar irradiation level [Fig. 15(b)].

Some waveforms are shown in Fig. 16 for the investigation of the tracking speed during the system power-on period. Fig. 16(a) shows that when the OCT technique is disabled, the settling time (t_s) for the system is 1.1 s. When the OCT technique is activated during the startup period, which can

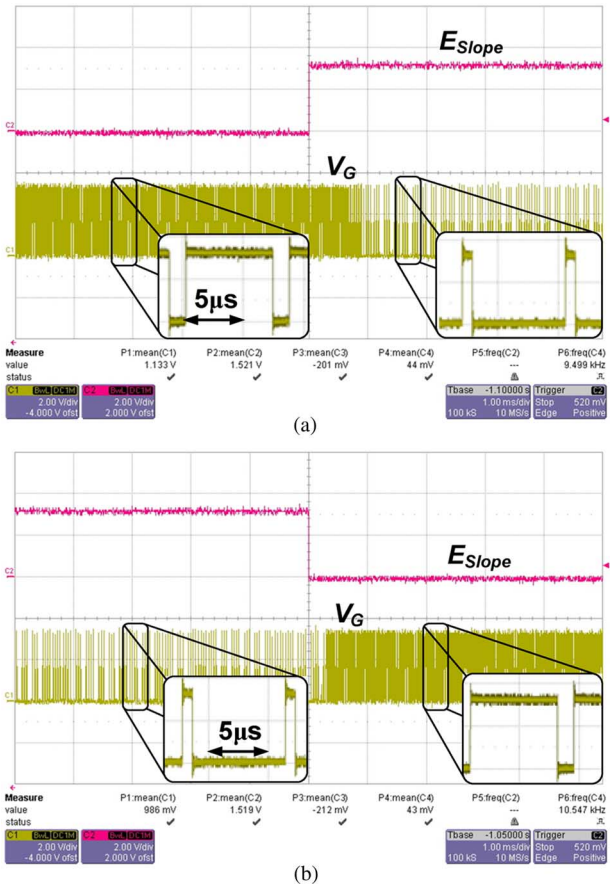

Fig. 15. Waveforms of V_G according to different E_{slope} values: (a) when the solar irradiation level increases, E_{slope} changes from low to high and (b) when the solar irradiation level decreases, E_{slope} changes from high to low.

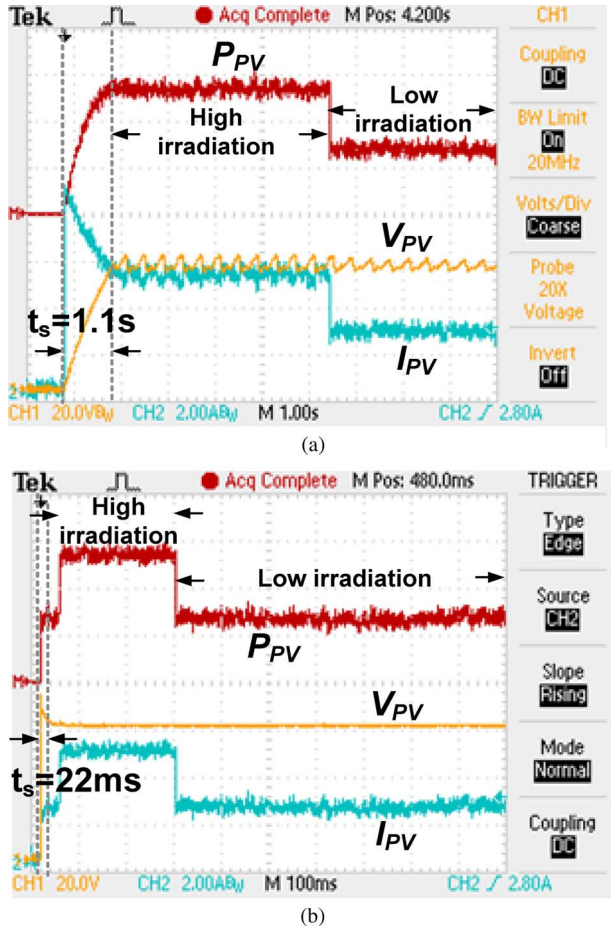

Fig. 16. Waveforms of $V_{\rm PV}$, $I_{\rm PV}$, and $P_{\rm PV}$ during the power-on period: (a) when the OCT technique is disabled and (b) when the OCT technique is activated.

rapidly approximate the MPP, the settling time can be shortened to 22 ms [Fig. 16(b)]. Therefore, the proposed MPPT algorithm and circuit improves tracking speed at the system startup period. Furthermore, the transient behavior during any environmental condition changes is also shown in Fig. 16. As can be seen in the figure, when the solar irradiation changes from high to low, the current transient time is less than 1 ms. The transient behavior on the dc bus is negligible since a large storage capacitor is connected.

Fig. 17 and Fig. 18 demonstrate some experimental results regarding the global maximum power point tracking. In Fig. 17, $E\%$ denotes the tracking accuracy degradation percentage, ΔP is the power variation due to the GMPPT, and $P_{\rm solar}$ is the energy provided by the solar arrays. As can be seen in the experimental result, the larger the power variation is the higher error percentage will be. The tracking error also incurs system efficiency degradation. T_{track} in Fig. 18 means the time the system takes to locate the GMPP. When the power variation increases, the system needs more time to track the GMPP.

Fig. 19 shows the waveforms at the dc-ac inverter output, which is connected to the boost converter as shown in Fig. 1. Fig. 20 demonstrates that when the grid-connected PV system is enabled, output voltage $V_{\rm ac}$ works in phase with grid power $V_{\rm Grid}$. Table II summarizes the measurement results. The proposed AMPPT achieves a tracking accuracy of higher than 97.3%.

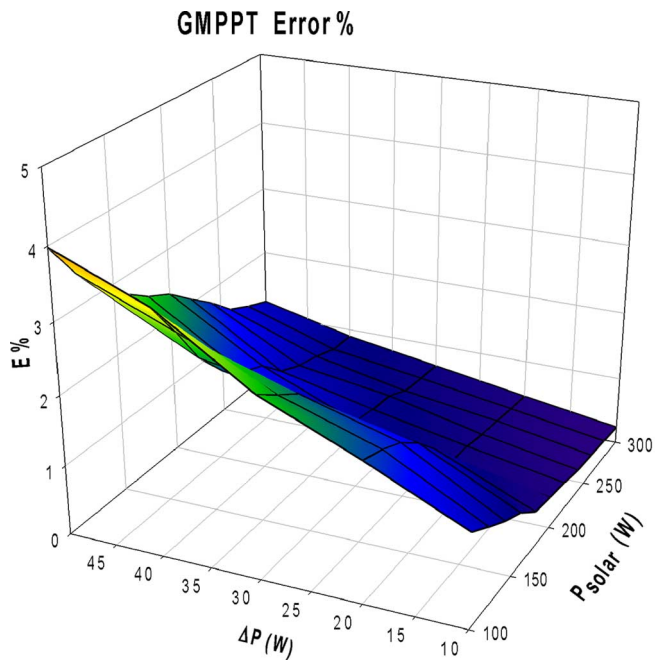

Fig. 17. GMPPT experiment results in terms of the tracking error percentage.

VI. Conclusion

The characteristic IV curves of the solar array are discussed to aid the understanding of the behaviors of solar arrays and de-

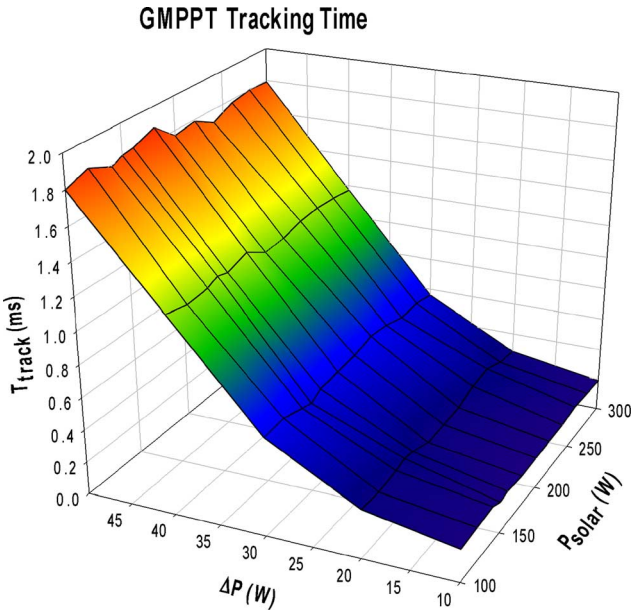

Fig. 18. GMPPT experiment results in terms of the tracking time.

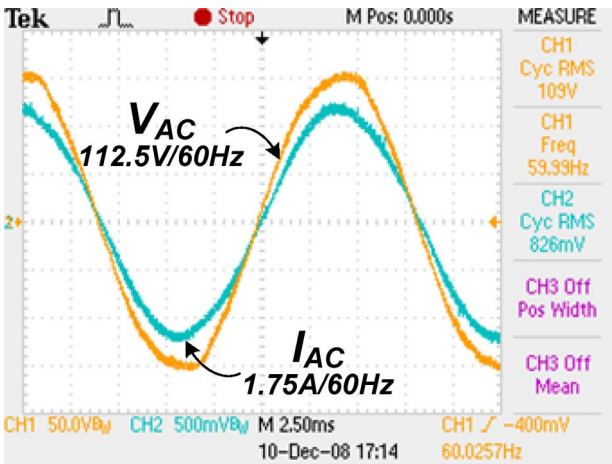

Fig. 19. Output voltage and current of the inverter.

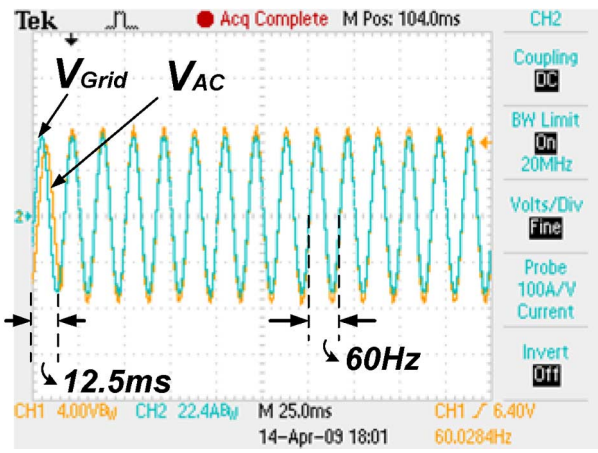

Fig. 20. Output waveforms when V_{ac} is connected to V_{Grid}.

sign the MPPT circuit. The proposed MPPT algorithm achieves fast tracking speed and maintains high tracking accuracy in the solar power system. Furthermore, with single-chip circuit implementation, power consumption can be reduced and the high power efficiency of the system is guaranteed. A wide-range current multiplier circuit is used to satisfy the requirement of the tracking circuit. The proposed MPPT circuit can determine the slope condition with fast speed and high accuracy. Experimental results verify the efficiency and tracking speed of the proposed MPPT algorithm. The findings also demonstrate that the PV system can convert solar energy into grid electricity with synchronized phase response. Moreover, a fully robust MPPT circuit can be applied when the GMPPT algorithm is included.

TABLE. II
DESIGN SPECIFICATIONS

Fabrication process	0.25μm BCD 40V 1P4M
Chip area	4.22 mm^2
Inductor	L_1=5 mH, L_2=5 mH
Capacitor	C_1=1500 μF, C_2=50 μF
Switching frequency	120 kHz
Nominal AC output voltage	112 V
Power factor	0.998
Tracking accuracy	>97.3% (@P_{PV}=100–285 W)
Overall power efficiency	88.97%
THD of current multiplier	1.02% (@I_{in}=30 μA, 100 kHz)
Operation range of current multiplier	0–60μA
Input capacitor	C_{pv}=4700 μF

ACKNOWLEDGMENT

The authors wish to thank Chunghwa Picture Tubes Ltd. for their help.

REFERENCES

[1] C.-Y. Hsieh and K.-H. Chen, "Boost DC-DC converter with Fast Reference Tracking (FRT) and Charge-Recycling (CR) techniques for high-efficiency and low-cost led driver," *IEEE J. Solid-State Circuits*, vol. 44, pp. 2568–2580, 2009.

[2] A. Richelli, L. Colalongo, S. Tonoli, and Z. M. Kovacs-Vajna, "A 0.2 V–1.2 V DC-DC boost converter for power harvesting applications," *IEEE Trans. Power Electron.*, vol. 24, pp. 1541–1546, 2009.

[3] E. Carlson, K. Strunz, and B. Otis, "20 mV input boost converter for thermoelectric energy harvesting," in *Proc. IEEE Symp. VLSI Circuits*, 2009, pp. 162–163.

[4] Z. Chen, J. M. Guerrero, and F. Blaabjerg, "A review of the state of the art of power electronics for wind turbines," *IEEE Trans. Power Electron.*, vol. 24, pp. 1859–1875, 2009.

[5] W. Rong-Jong and W. Wen-Hung, "Grid-connected photovoltaic generation system," *IEEE Trans. Circuits Syst. I, Reg. Papers*, vol. 55, pp. 953–964, 2008.

[6] G. J. Bauhuis *et al.*, "26.1% thin-film GaAs solar cell using epitaxial lift-off," *Solar Energy Mater. Solar Cells*, vol. 93, pp. 1488–1491, 2009.

[7] M. A. Green *et al.*, "Solar cell efficiency tables (version 36)," *Progr. Photovoltaics: Res. Appl.*, vol. 18, pp. 346–352, 2010.

[8] T. Esram, J. W. Kimball, P. T. Krein, P. L. Chapman, and P. Midya, "Dynamic maximum power point tracking of photovoltaic arrays using ripple correlation control," *IEEE Trans. Power Electron.*, vol. 21, pp. 1282–1291, 2006.

[9] S. Jain and V. Agarwal, "A single-stage grid connected inverter topology for solar pv systems with maximum power point tracking," *IEEE Trans. Power Electron.*, vol. 22, pp. 1928–1940, 2007.

[10] F. Boico, B. Lehman, and K. Shujaee, "Solar battery chargers for NiMH batteries," *IEEE Trans. Power Electron.*, vol. 22, pp. 1600–1609, 2007.

[11] T. Esram and P. L. Chapman, "Comparison of photovoltaic array maximum power point tracking techniques," *IEEE Trans. Energy Convers.*, vol. 22, pp. 439–449, 2007.

[12] C. Rodriguez and G. A. J. Amaratunga, "Analytic solution to the photovoltaic maximum power point problem," *IEEE Trans. Circuits Syst. I, Reg. Papers*, vol. 54, pp. 2054–2060, 2007.

[13] J.-M. Kwon, B.-H. Kwon, and K.-H. Nam, "Three-phase photovoltaic system with three-level boosting MPPT control," *IEEE Trans. Power Electron.*, vol. 23, pp. 2319–2327, 2008.
[14] N. Khaehintung, T. Wiangtong, and P. Sirisuk, "FPGA implementation of MPPT using variable step-size P&O algorithm for PV applications," in *Proc. Int. Symp. Commun. Inf. Technol. (ISCIT)*, 2006, pp. 212–215.
[15] W. Wu, N. Pongratananukul, W. Qiu, K. Rustom, T. Kasparis, and I. Batarseh, "DSP-based multiple peak power tracking for expandable power system," in *Proc. IEEE Appl. Power Electron. Conf. Expo.*, 2003, vol. 1, pp. 525–530.
[16] Z. Liang, R. Guo, and A. Huang, "A new cost-effective analog maximum power point tracker for PV systems," *Proc. IEEE Energy Convers. Congr. Expo. (ECCE)*, pp. 624–631, 2010.
[17] P. Mattavelli, S. Saggini, E. Orietti, and G. Spiazzi, "A simple mixed-signal MPPT circuit for photovoltaic applications," in *Proc. IEEE Appl. Power Electron. Conf. Expo.*, 2010, pp. 953–960.
[18] K. K. Tse, M. T. Ho, H. S.-H. Chung, and S. Y. Hui, "A novel maximum power point tracker for PV panels using switching frequency modulation," *IEEE Trans. Power Electron.*, vol. 17, pp. 980–989, 2002.
[19] H. S.-H. Chung, K. K. Tse, S. Y. R. Hui, C. M. Mok, and M. T. Ho, "A novel maximum power point tracking technique for solar panels using a SEPIC or Cuk converter," *IEEE Trans. Power Electron.*, vol. 18, pp. 717–724, 2003.
[20] R. Leyva, C. Alonso, I. Queinnec, A. Cid-Pastor, D. Lagrange, and L. Martinez-Salamero, "MPPT of photovoltaic systems using extremum—Seeking control," *IEEE Trans. Aerosp. Electron. Syst.*, vol. 42, pp. 249–258, 2006.
[21] J.-H. Park, J.-Y. Ahn, B.-H. Cho, and G.-J. Yu, "Dual-module-based maximum power point tracking control of photovoltaic systems," *IEEE Trans. Ind. Electron.*, vol. 53, pp. 1036–1047, 2006.
[22] D. Brunelli, C. Moser, L. Thiele, and L. Benini, "Design of a solar-harvesting circuit for batteryless embedded systems," *IEEE Trans. Circuits Syst. I, Reg. Papers*, vol. 56, pp. 2519–2528, 2009.
[23] A. Tariq and J. Asghar, "Development of an analog maximum power point tracker for photovoltaic panel," in *Proc. Int. Conf. Power Electron. Drives Syst.*, 2005, pp. 251–255.
[24] D. Sera, T. Kerekes, R. Teodorescu, and F. Blaabjerg, "Improved MPPT algorithms for rapidly changing environmental conditions," in *Proc. Power Electron. Motion Control Conf. (EPE-PEMC)*, 2006, pp. 1614–1619.
[25] C.-X. Liu and L.-Q. Liu, "An improved perturbation and observation MPPT method of photovoltaic generate system," in *Proc. IEEE Conf. Ind. Electron. Appl. (ICIEA)*, 2009, pp. 2966–2970.
[26] G. J. Yu, Y. S. Jung, J. Y. Choi, I. Choy, J. H. Song, and G. S. Kim, "A novel two-mode MPPT control algorithm based on comparative study of existing algorithms," in *Conf. Rec. 29th IEEE Photovoltaic Specialists Conf.*, 2002, pp. 1531–1534.
[27] C. Dorofte, U. Borup, and F. Blaabjerg, "A combined two-method MPPT control scheme for grid-connected photovoltaic systems," in *Proc. Eur. Conf. Power Electron. Appl.*, 2005, p. 10.
[28] Y.-M. Chen, H.-C. Wu, Y.-C. Chen, K.-Y. Lee, and S.-S. Shyu, "The AC line current regulation strategy for the grid-connected PV system," *IEEE Trans. Power Electron.*, vol. 25, pp. 209–218, 2010.
[29] P. Maffezzoni and D. D'Amore, "Compact electrothermal macromodeling of photovoltaic modules," *IEEE Trans. Circuits Syst. II, Exp. Briefs*, vol. 56, pp. 162–166, 2009.
[30] M. G. Villalva, J. R. Gazoli, and E. R. Filho, "Comprehensive approach to modeling and simulation of photovoltaic arrays," *IEEE Trans. Power Electron.*, vol. 24, pp. 1198–1208, 2009.
[31] N. Femia, G. Petrone, G. Spagnuolo, and M. Vitelli, "Optimization of perturb and observe maximum power point tracking method," *IEEE Trans. Power Electron.*, vol. 20, pp. 963–973, 2005.
[32] M. A. Masoum, H. Dehbonei, and E. F. Fuchs, "Theoretical and experimental analyses of photovoltaic systems with voltageand current-based maximum power-point tracking," *IEEE Trans. Energy Convers.*, vol. 17, pp. 514–522, 2002.
[33] T. Shimizu, M. Hirakata, T. Kamezawa, and H. Watanabe, "Generation control circuit for photovoltaic modules," *IEEE Trans. Power Electron.*, vol. 16, pp. 293–300, 2001.
[34] H. Patel and V. Agarwal, "Maximum power point tracking scheme for PV systems operating under partially shaded conditions," *IEEE Trans. Ind. Electron.*, vol. 55, pp. 1689–1698, 2008.
[35] Tynsolar [Online]. Available: http://www.tynsolar.com.tw/upload/TYN-285P6.pdf
[36] H. Patel and V. Agarwal, "MPPT scheme for a PV-fed single-phase single-stage grid-connected inverter operating in CCM with only one current sensor," *IEEE Trans. Energy Convers.*, vol. 24, pp. 256–263, 2009.
[37] RefuSol, "Königsmörder," *Photon Profi, Photovoltaik-Fachwissen für Praxis* vol. 51, 2010 [Online]. Available: http://www.photon.info

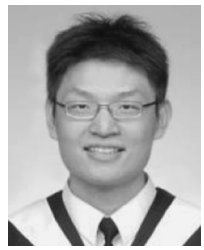

Chih-Yu Yang was born in Kaohsiung, Taiwan. He received the B.S. and M.S. degrees in electrical and control engineering from National Chiao Tung University, Taiwan, in 2008 and 2011, respectively.

His research interests include design of power management circuit, LED driver ICs, solar battery charger, and analog integrated circuit designs.

Chun-Yu Hsieh was born in Taichung, Taiwan. He received the B.S. and Ph.D. degrees from the Department of Electrical and Control Engineering, National Chiao Tung University, Taiwan, in 2006 and 2010, respectively.

His research area includes many projects of LED driver ICs and power management ICs at Low Power Mixed Signal Lab now. He is the author or coauthor of more than 20 papers published in journals and conferences, and also holds several patents. His interests include power management circuit designs, LED driver ICs, and analog integrated circuit designs.

Fu-Kuei Feng was born in Taipei, Taiwan. He received the M.S. degree in electrical and control engineering from National Chiao Tung University, Hsinchu, Taiwan, in 2009.

He has been engaged in design and development of PV inverters, UPS, power inverters, and solar chargers for 23 years. His research interests are in the areas of power electronics, digital control systems, and renewable energy converter.

Ke-Horng Chen (M'04–SM'09) received the B.S., M.S., and Ph.D. degrees in electrical engineering from National Taiwan University, Taipei, in 1994, 1996, and 2003, respectively.

From 1996 to 1998, he was a part-time IC designer at Philips, Taipei. From 1998 to 2000, he was an application engineer at Avanti Ltd., Taiwan. From 2000 to 2003, he was a project manager at ACARD Ltd., where he was engaged in designing power-management ICs. He is currently a Professor in the Department of Electrical Engineering, National Chiao Tung University, Hsinchu, Taiwan, where he oversees the Mixed-signal and Power Management IC Laboratory. He is the author and coauthor of more than 100 papers published in journals and conferences, as well as the owner of several significant patents. His current research interests include power management ICs; mixed-signal circuit designs; display algorithm and driver designs of liquid crystal display TV; red, green, and blue color sequential backlight designs for optically compensated bend panels; and low-voltage circuit designs.

Dr. Chen has served as an Associate Editor of the IEEE TRANSACTIONS ON POWER ELECTRONICS and the IEEE TRANSACTIONS ON CIRCUITS AND SYSTEMS—PART II. He is on the IEEE CAS VLSI Systems and Applications Technical Committee and the IEEE CAS Power and Energy Circuits and Systems Technical Committee.